

Electrochemical performance of composites made of rGO with Zn-MOF and PANI as electrodes for supercapacitors

Le Quoc Bao^{a,b*}, Thanh-Huong Nguyen^c, Haojie Fei^a, Irina Sapurina^a, Fahanwi Asabuwa Ngwabebhoh^{a,g}, Constantin Bubulinca^a, Lukas Munster^a, Eva Domincová Bergerová^a, Anezka Lengalova^a, Hao Jiang^d, Tran Trong Dao^e, Nikola Bugarova^f, Maria Omastova^f, Natalia E. Kazantseva^{a,h}, Petr Saha^{a,g,h}

^a University Institute, Tomas Bata University in Zlín, Nad Ovcirnou IV 3685, 760 01, Zlín, Czech Republic.

^b Conducting Polymers in Composites and Applications Research Group, Faculty of Applied Sciences, Ton Duc Thang University, Ho Chi Minh City, Vietnam.

^c Center of Excellence for Green Energy and Environmental Nanomaterials, Nguyen Tat Thanh University, 300A Nguyen Tat Thanh, District 4, Ho Chi Minh City 755414, Vietnam

^d Key Laboratory for Ultrafine Materials of Ministry of Education, Shanghai Engineering Research Center of Hierarchical Nanomaterials, School of Materials Science and Engineering, East China University of Science and Technology, Shanghai 200237, China.

^e Division of Modeling Evolutionary Algorithms Simulation and Artificial Intelligence, Faculty of Electrical & Electronics Engineering, Ton Duc Thang University, Ho Chi Minh City, Vietnam.

^f Polymer Institute, Slovak Academy of Science, Dubravska cesta, 9, 845 41 Bratislava, Slovakia

^g Footwear Research Centre, Tomas Bata University in Zlín, Nad Ovcirnou IV 3685, 760 01, Zlín, Czech Republic.

^h Faculty of Technology, Tomas Bata University in Zlin, Vavrečkova 275, 760 01 Zlin, Czech Republic.

Abstract

Metal-organic frameworks (MOFs) have lately obtained great attention of scientists as potential materials applied for supercapacitor electrodes. Due to their crystalline structure, MOFs show proper electrochemical double-layer capacitance at the enlarged specific surface area of the material and the mechanical supports for the composite materials. In this study, Zn-MOF was synthesized and composited with reduced graphene oxide (rGO) to be applied as a supercapacitor

electrode material. To improve the electrodes working performance, polyaniline (PANI) was synthesized by different methods and added to the composite. The electrochemical properties of these materials were studied to identify the effect of PANI and Zn-MOF on the electrode materials. Among the composites obtained, the best specific capacitance of about 372 F/g was obtained at 0.1 A/g charge-discharge analysis of rGO/Zn-MOF@PANI sample due to its large surface with high pores sizes. The capacitance retentions of electrodes were also tested to decipher the effect caused by varied composites fabrication.

Keywords: Supercapacitor, Zn-metal-organic framework, Conductive polymer, Composite material, Reduced graphene oxide, Electrode.

1. Introduction

In recent years, environmental pollution has become a global problem. One of the reasons for this phenomenon is associated with an increase in energy demand, which entails a higher consumption of fossil fuels. Consequently, research towards efficient renewable energy sources and the growing demand for them has given a renewed impetus to improving electric energy storage devices [1–5]. The electrochemical supercapacitor (SC) is one of the promising types of power source devices. It plays a vital role in recent technology applications due to its advantages such as high power density, good reversibility, long cycle life, and high intrinsic safety [6,7]. For the design of SC electrodes, carbon-based materials [8], transition metal oxides/hydroxides [9], and conductive polymers [10] are mostly used. The application of these materials increases the capacity of SCs due to the presence of the Faradaic reactions and the separation of charge between the electrode-electrolyte interfaces [1,11].

Carbon-based materials, e.g., graphene oxide (GO) or reduced graphene oxide (rGO), have shown good electrical properties and have been widely investigated as components of SCs. However, they have several drawbacks such as low specific surface area and difficult fabrication,

which hinder their application in SC [12]. Many efforts have been made to overcome these problems, such as developing nano-carbon materials or making composites of carbon matrix with various reinforcements. Although SCs based on nanomaterials have shown impressive electrochemical performance in laboratory conditions, their preparation methods are too challenging to apply in the mass production. One of the leading research directions is developing composite materials that should combine the advantages of their components [13].

One of the potential materials for SC application investigated for a long time is polyaniline (PANI). As a conducting polymer, it exhibits many useful properties: good reversibility, electrical conductivity, which can be controlled by synthesis conditions, secure processing, and what is more critical, pseudocapacitance [14–16]. However, PANI demonstrates poor cyclic stability due to the polymer's mechanical destruction during the doping-undoping process, which has limited the application of PANI through charge-discharge processes in long periods [17].

This work aims to improve the specific super-capacitance while increasing the cyclic stability of SC using composite materials based on rGO, PANI, and zinc-based metal-organic frameworks (Zn-MOFs). To this end, different composites were fabricated to investigate their working performance as electrode materials. Metal-organic frameworks (MOFs) created by organic linkers and metal ions have long been considered coordination polymers with porous features, including large specific surface area, high stability, and organic functionality. These characteristics have led to their advanced usability in electrochemical devices [18–20].

Moreover, a wide selection of metal ions and organic linkers provides thousands of MOF variations for different potential applications. Indeed, a variety of metal ions dealing with the electrochemical properties of MOFs in SC have been identified, such as Zr- [21], Fe- [22], Co- [23], In- [24], Mn- [25, 26], Zn- and Cd- [20]. Among the various metals, Zn has been commonly

used to make a composite with rGO and a conductive polymer in order to obtain good SC performance [27]. For example, Zn-MOF application on SC was reported by Lin and his coworkers [20]; their results showed that the material could provide excellent cyclic stability. It exhibited larger capacitances than a bare carbon glassy electrode.

In this study, the composites of rGO, PANI, and Zn-MOF were prepared via the one-step co-assembly method, i.e., PANI prepared at different synthesis conditions was supported on the composite structure of rGO and Zn-MOF. The electrochemical properties of the materials thus obtained were studied to determine their performance for the use as an electrode material for SC.

2. Experimental

2.1. Materials

Synthetic graphite powder ($< 20 \mu\text{m}$), potassium permanganate ($\text{KMnO}_4 \geq 99.0\%$), ammonium persulfate ($(\text{NH}_4)_2\text{S}_2\text{O}_8, \geq 98.0\%$), aniline, zinc nitrate hexahydrate ($\text{Zn}(\text{NO}_3)_2 \cdot 6\text{H}_2\text{O}$), terephthalic acid (H_2BDC , 98%), N, N'- dimethylformamide and perchloric acid (HClO_4 , 70%) were products of Sigma-Aldrich. Sulfuric acid (96%), hydrogen peroxide solution (30%), and all solvents were purchased from local companies PENTA and VWR Chemicals. All the chemicals were used without any further purification.

2.2. PANI preparation

Firstly, 0.02 mol of aniline and 0.025 mol of ammonium persulfate were separately mixed in 50 mL HCl solution (0.2 M) and stirred continuously until discrete homogeneous solutions were obtained. After that, the ammonium persulfate solution was slowly poured into the aniline solution. The mixture was kept at room temperature for 48 h before filtration. The residue was then washed

many times with distilled water and methanol. Finally, the residue was dried in a vacuum oven for 12 h to receive dark green polyaniline powder (PANI(p)).

2.3. GO preparation

Graphene oxide was prepared according to Hummers' method. Firstly, a four-neck flask containing 3 g of graphite powders was put in an ice bath. Then, 75 mL H₂SO₄ (96%) was slowly added to the flask, and the suspension was stirred for 1 h. Next, 9 g of KMnO₄ was slowly added to the mixture under continuous stirring. After 3 h, 100 mL of deionized (DI) water was dropped slowly to the mixture, then, an additional 150 mL of DI water was added. Finally, 20 mL of hydrogen peroxide (30%) was slowly poured to the mixture and stirred for 30 min on the ice bath. Subsequently, the mixture was washed with DI water and centrifuged until its pH was approximately neutral. GO was then freeze-dried and kept in cold conditions for further experiments.

2.4. Synthesis of Zn-MOFs

Zn-MOFs were synthesized following the typical procedure described in [28]. Zn(NO₃)₂·6H₂O (14.87 g, 50 mmol) and H₂BDC (1.672 g, 10 mmol) were dissolved in 60 mL of dimethylformamide (DMF). The mixture was stirred until complete dissolution. The mixture was then transferred into 80 mL Teflon-lined stainless steel autoclave, which was heated up to 120 °C for 20 h then cooled to room temperature. The crystallites were collected and washed several times with methanol and DMF before being centrifugated at 4000 rpm for 30 min. The obtained residue was activated by removing the solvent under vacuum at 100 °C over 12 h.

2.5. Synthesis of partial composites

Three types of composites were prepared in this step (herein labeled **G1**, **G2**, **G3**). The first one, rGO/Zn-MOF aerogel (**G1**), was synthesized using a one-step hydrothermal co-assembly method [29]. Firstly, Zn-MOF (0.02 g) and GO (0.1 g) were dispersed in 5 mL DI water to make a suspension. The mixture was sonicated for 60 min, and the content was then transferred to an autoclave, which was heated to 160 °C for 5 h subsequently cooled to room temperature. The hybrid hydrogel was collected, washed several times with DI water, and kept in 10 mL of DI water. A similar procedure was applied in the preparation of rGO/PANI(p) (**G2**); however, instead of Zn-MOF, previously prepared PANI(p) (0.02 g) was used. To make rGO/PANI(p)/Zn-MOF (**G3**), the mixture of Zn-MOF (0.02 g), PANI(p) (0.02g), and GO (0.1 g) was prepared following a similar procedure. All the hybrid composites were freeze-dried to receive **G1**, **G2** and **G3**.

2.6. Preparation of the final composite

In the preparation of the final composite, **G1** was modified via the in situ polymerization [30]. A piece of synthesized graphene hydrogel was immersed in 50 mL of DI water in a 100 mL beaker, and then 1.5 mL of aniline was added. The beaker was covered and kept at room temperature for 2 h. This step was repeated before the piece of aerogel was immersed in 50 mL solution of perchloric acid (6.8%) for 18 hours. The solution was then removed, and the piece was immersed in the solution of perchloric acid (9.2 %, 22 mL) and kept at 0°C for 1 h. Then, the solution of ammonium persulfate (17.5 mM, 10 mL) was dropped slowly to a solution of perchloric acid under continuous stirring. The piece was kept in the solution at 0°C for 48 h to polymerize. After that, the beakers were taken out and kept at room temperature for 24 h. The resulting composite was washed several times with DI water and then freeze-dried to receive rGO/Zn-MOF@PANI (**G4**).

2.7. Characterization techniques

The crystal structure of Zn-MOF was analyzed via X-ray powder diffraction (XRD) patterns employing a Cu-K α radiation source from a D8 Advance Bruker powder diffractometer. The chemical composition was identified by ATR-FTIR spectroscopy by using Nicolet iS10 (Thermo Scientific) equipped with an ATR sampling accessory with a Ge crystal plate. The carbon, hydrogen, and nitrogen contents of the composites were determined by elemental analysis (EA). The material morphologies were characterized by a NANOSEM 450 (FEI, USA) scanning electron microscope (SEM) operated at 5 kV under 90 Pa pressure. The prepared samples were also investigated by transmission electron microscopy (TEM) employing the JEOL JEM-2100 electron microscope (JEOL, Japan) operated at 160 kV accelerating voltage. The samples were ultrasonically dispersed in water (0.5 wt%), drop-cast onto formvar coated 300 mesh copper grids, and gently dried. The specific surface areas were calculated according to Brunauer–Emmett–Teller (BET) method. Nitrogen physisorption measurements were conducted by using the Micromeritics 2020 volumetric adsorption analyzer system and all samples were undergone the heat pretreatment under vacuum at 150 °C for 3 h.

The determination of C, H, N, was conducted by the FLASH method. The amount of each element was evaluated in percentage by weight (% m/m). It is a destructive method since the samples will be burnt during the process (the Dumas method of combustion, 960 °C). Samples were measured (2-3 mg) and packed into silver capsules and placed inside the instrument. Each sample was analyzed 3 times in two measurements for the determination of RSD value. Values were given in percent by weight (% m/m). The standard sample was sulphanilamide. The reaction products were CO₂, N₂, H₂O and SO₂, which were then carried by the helium flow through the separation gas chromatographic column, where they were detected by the TCD detector based on

the calibration curve of the standards and identified by the instrument software. The content of elements in the samples was determined by the EDX-XRF method (Energy ray dispersion spectroscopy - X-ray fluorescence), which was based on the elemental analysis of X-ray diffraction (energy) materials. Each element has a different X-ray energy radiation, by type and quantum of X-ray. Radiation was determined by the type and amount of element in the sample.

Thermogravimetric analysis (TGA) measurements were conducted with a heating rate of 10 °C/min under the nitrogen atmosphere, ranging from 28 to 900 °C. TGA curves were recorded with a thermo-gravimetric and differential thermal analyzer SETARAM LabSys Evo TG-DSC 1600 (SETARAM Instrumentation, France).

To analyze the chemical composition and binding energy of the composites obtained, X-ray Photoelectron Spectroscopy (XPS) was applied. The measurements were carried out by using the photoelectron spectrometer Hemo Scientific™ K-Alpha XPS system (Thermo Fisher Scientific) with a monochromatic Al K α source, pass energies of 200 eV (step size 1.0 eV) and 30 eV (step size 0.1 eV) for the survey and high-resolution spectra, respectively.

2.8. Fabrication of working electrodes and their electrochemical testing

The electrochemical test was performed by making a slurry with the crushed composite with a solution of PTFE (10% of total mass) in 1 ml ethanol. The slurry was coated as a circle of 0.25 cm radius on the titanium mesh and then compressed under the pressure of 8 MPa. The as-prepared electrodes' electrochemical performance was characterized using cyclic voltammetry (CV), galvanostatic charge-discharge tests, and electrochemical impedance spectroscopy (EIS) techniques on a potentiostat Autolab PGSTAT-128 N at room temperature. Electrochemical measurements were performed in a three-electrode cell using a working electrode, a platinum wire

with high area dimension electrode, and an Ag/AgCl reference electrode. The measurements were carried out in an aqueous solution of two different electrolytes of 1 M H₂SO₄ at room temperature.

Electrochemical impedance spectroscopy (EIS) measurements were conducted on aerogel structure coated electrodes in a constant voltage mode (0.02 V vs. Ag/AgCl) by sweeping frequencies from 100 kHz to 0.01 Hz at an amplitude of 0.01 V_{RMS}.

In the two-electrode system, two same electrodes were compressed in a Swagelok cell and separated by a piece of supercapacitor separator (NKK-MPF30AC).

The cycling stability of the prepared materials was measured in a two-electrode system by BioLogic battery cyclers (BCS-810) at the current density of 1 A/g for 5000 times.

3. Results and discussion

3.1. Morphology and surface analysis

Zn-MOFs and PANI(p) morphologies are shown in **Fig. S1**. The SEM image of PANI(p), as shown in **Fig. S1(a)**, displays nano-granules of spherical shape. The formation of PANI with such morphology can be caused by strong interactions between conjugated polymer chains [10]. The SEM image in **Fig. S1(b)** displays the crystalline structure of Zn-MOF. As can be seen in **Fig. S2(a)**, the XRD pattern of Zn-MOF shows sharp peaks at 5.56° and 15.92° corresponding to the crystalline planes of (200) and (420), respectively. The high intensity of these peaks is related to the prepared compound's high crystallinity and consistency [31]. **Fig. S2(b)** displays the molecular structure and atom-labeling scheme of Zn-MOF. A zinc ion's local coordination is a distorted tetrahedron completed by oxygen atoms from BDC [32–34].

The morphologies of composites **G1**, **G2**, **G3**, and **G4** obtained via hydrothermal reaction in the autoclave, are shown in **Fig. 1**. During the hydrothermal reaction process at a high temperature,

GO reduces to rGO with sheets morphology. The sheets contain hydrophobic basal planes and hydrophilic edges, which can act as a surfactant. During the reaction, an internal large lateral dimension and an array of hydrophobics were created. The π -conjugated nano patches in the basal planes were formed as rGO sheets, which captured Zn-MOF or PANI(p) particles into their multiple adhesion sites [10]. Besides, all the composites show excellent 3D porous structures caused by the graphene sheets, which could enhance the electrolyte ion-adsorption ability [35].

The TEM images of **G1** (**Fig. 1e** and **f**) clearly indicate that Zn-MOF particles are remarkably consistent over the surface of each rGO sheet. The good dispersion of Zn-MOFs in **G1** shows the development of graphene sheets based on Zn-MOF crystalites. This provides outstanding aerostability, prevents aggregation and may increase the surface area as well. **Fig. 1g** and **h** display the distribution of PANI(p) inside sample **G2**. It can be seen that PANI(p) granules are aggregated together, which would lead to the decrease of surface area inside this composite. Similarly, TEM images of **G3** (**Fig. 1i** and **j**) also show PANI(p) accumulation inside the sample. Consequently, TEM images of **G4** show that PANI has been synthesized as thin-film inside the scaffold (**Fig. 1k** and **l**). The different appearance of PANI in **G4** compared to other composite materials may be ascribed to the distinct formation methods. The PANI's thin-film layers in **G4** created by in situ polymerization process would enhance the exfoliation of rGO sheets. Hence that would create excellent interaction among each component, which may contribute to enhance the SC capacitance. However, because the physical flexibility of PANI films is low [Ref], the synthesized PANI in **G4** can also affect to the cyclic stability of the sample. The aggregation of PANI(p) inside **G2** and **G3**, may restrain the interactions between the surface of materials and electrolytes in electrochemical applications, which may not happen in **G4** due to the thin-film layer appearance.

The specific surface areas and porosities of electrode materials were elucidated through BET method, as displayed in **Fig. 2**. The literature review indicated that the surface area could be significantly increased by the combination of PANI and rGO compared to each particular component [36]. The **G2** sample shows a corresponding result of about 57.82 m²/g, which is higher than conventional rGO materials [37]. The addition of the porous material as Zn-MOF instead of PANI in **G1** makes the specific surface area risen to 79.88 m²/g. The combination of Zn-MOF, rGO and two kinds of PANI bring a considerable difference in surface area with 140.97 and 53.12 m²/g for **G3** and **G4**, respectively. It would be ascribed to the mixed-method, causing the increase in result of **G3**, whereas the synthesized polymer making that of **G4** declined remarkably. The thin-layer of PANI formed during in-situ polymerization could cover Zn-MOF crystallites and partially the surface area of rGO. Therefore the specific surface area of **G4** was recorded as the smallest.

3.2. Fourier transforms infrared spectroscopy, elemental analysis, and thermogravimetric analysis

Fourier transforms infrared (FTIR) spectra of Zn-MOF synthesized via the solvothermal method, and those of PANI(p) are shown in **Fig. 3a**. In the spectrum of Zn-MOF, the signal at 3608 cm⁻¹ and 3362 cm⁻¹ displays the -OH stretching. The asymmetric vibration of -COO is shown at 1560 cm⁻¹, and the peak at 1370 cm⁻¹ corresponds to the asymmetric and symmetric stretch of carboxylate groups. The peaks at 1149 cm⁻¹, 1103 cm⁻¹, and 1017 cm⁻¹ correspond to C-C vibration. The FTIR spectrum of the prepared PANI(p) shows a characteristic peak at 3400 cm⁻¹, which is assigned to the N-H stretching vibration of PANI's amino group. The

absorption band at 2465 cm^{-1} corresponds to N-H unsaturated amine. The peaks at 1567 cm^{-1} and around 1600 cm^{-1} show the stretching vibration of amine atoms and the benzenoid ring.

After oxidization via thermal reaction, graphene flakes contain oxygen-groups in their structures (**Fig. 3b**). The OH stretching of the hydroxyl group of GO is displayed via peaks at $3434 - 3391\text{ cm}^{-1}$. The FTIR spectrum of GO is shown in **Fig. 3b**; broadband at 3354 cm^{-1} is related to the -OH group's intense stretching. A peak at 1580 shows the stretching vibration of C=C. The peaks at 1731 , 1171 , and 1044 cm^{-1} are corresponded to the stretchings of C=O, C-OH, and C-O, respectively. When GO is reduced to rGO, carbonyl groups (C=O) are reduced to methylene (-CH₂-). The peaks at 2983 and 2901 cm^{-1} in all spectra show the symmetric and asymmetric stretching vibration of -CH₂-, respectively [38]. The C=O stretching vibration of sp² carbon due to the carboxylic group site at the edge of GO is identified via the peaks at 1726 cm^{-1} . The strong peaks at 1566 cm^{-1} represent the aromatic C=C in-plane vibrations. Further, the peaks at 1206 cm^{-1} and 1087 cm^{-1} are caused by C-O stretching vibrations and the carbonyl groups leftover after reduction [10,36].

The elemental analysis was carried out to find different elements and their distribution in the synthesized composites, and the results are presented in **Table 1**. The main components of these composites are C, H and N. The amount of N in the composites indicates the presence of PANI. As can be seen from **Fig. S3**, all elements are evenly distributed throughout the composites. The results of **Table 1** and **Fig. S3** confirm that N is not present on the composite of **G1**, the spectra only show the peaks of C and H. In contrast, when PANI(p) is present as a component of the aerogel composite, the percentages of N in **G2** and **G3** are 1.63% and 1.8%, respectively. Thus, it has been proven that the prepared composites contain PANI. The elemental analysis of **G4** displays 0.5% of N, which confirms the presence of PANI in this composite too.

The thermal stability of **G1**, **G2**, **G3**, and **G4** composites was investigated by TGA at a scan rate of $10\text{ }^{\circ}\text{C min}^{-1}$ under N_2 atmosphere up to $900\text{ }^{\circ}\text{C}$ (**Fig. 4**). As can be seen, when the temperature rises to $100\text{ }^{\circ}\text{C}$, composites initially lose $1.15\% \sim 3.78\%$ of their weight due to physically absorbed water molecules. Sample **G1** shows a significant loss of weight from $250 - 900\text{ }^{\circ}\text{C}$ due to the decomposition of Zn-MOF, for which the ratio of Zn-MOF and GO suspension during the synthesis was 1:5. The percentage loss in the TGA result agrees well with this ratio.

TGA curve of **G2** shows a step weight loss from $170 - 299\text{ }^{\circ}\text{C}$, where the doped hydrochloric acid bounded to PANI chains is eliminated, and PANI is decomposed. The mass of the sample is stable until the oxidative degradation of the PANI backbone starts at $428\text{ }^{\circ}\text{C}$ [39]. The sample is wholly oxidized at about $523\text{ }^{\circ}\text{C}$, and the weight loss of **G2** is 5.364% . TGA curves of **G3** and **G4** also show the combined phenomenons of **G1** and **G2** due to the content of both Zn-MOF and PANI. The initial weight loss patterns around $100\text{ }^{\circ}\text{C}$ are mainly assigned to the loss of bound water molecules from the structures. The curves also show the step weight loss starting around $170\text{ }^{\circ}\text{C}$, which is assigned to the elimination of acid backbone in PANI. When the temperature increases to $250\text{ }^{\circ}\text{C}$, the decomposition of Zn-MOF starts. The weight percentage of **G3** reaches constant at 81.13% above $525\text{ }^{\circ}\text{C}$. The residue weight of **G4** is approximately 78.85% above $778\text{ }^{\circ}\text{C}$. The results are in good agreement with the elemental analysis, which proved the amount of PANI synthesized in **G4** smaller than PANI(p) in **G3**.

3.3. X-ray photoelectron spectroscopy

XPS was applied to analyze the surface composition of prepared hybrids. The survey scans are shown in **Fig. 5a**, which confirms the presence of Zn ($\text{Zn}2p_{3/2}$, $\text{Zn}2p_{1/2}$), O ($\text{O}1s$), C ($\text{C}1s$), and N ($\text{N}1s$) in the samples. The high-resolution spectra of the $\text{Zn}2p$ of the Zn-MOF region are shown

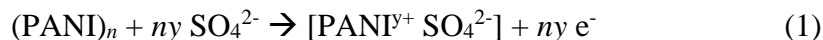
in **Fig. S4**. The specific peaks located at about 1021 eV ($\text{Zn}2p_{3/2}$) and 1045 eV ($\text{Zn}2p_{1/2}$) are shown similarly between samples **G1**, **G3**, and **G4** (**Fig. S5a**). The absence of loss feature in $\text{Zn}2p$ spectra and broader $\text{Zn}2p_{3/2}$ peak prove the Zn^{2+} (ZnO), as well as the shift of Auger peak at Kinetic energy from 990eV to 987 eV (**Fig. S4e**). The appearance of $\text{Zn}2p$ peaks in samples confirmed the existence of Zn-MOF in composites [40]. **Fig. 5b** shows the high-resolution spectra of $\text{C}1s$ for the C-C bond (284.46 eV) for all samples. This peak is assigned to sp^2 hybridized carbon present in the aromatic ring. The slight increase at 285.42 eV corresponding to C-N group was acquired from **G2**, **G3**, and **G4**, indicating the existence of PANI in the composites. In the $\text{C}1s$ spectra of all samples, the peaks of C-O (286.12 eV), C=O (287.30 eV) and OC=O (288.80 eV) were also found [41]. The highest binding energy peaks positioned at 291.46 eV (labeled as $\pi-\pi^*$) confirmed the presence of delocalized π electrons (conduction electrons) available for shake-up like events following core electron photoemission typical for aromatic rings of rGO as well as PANI. As shown in **Fig. 5c**, The XPS spectra of $\text{O}1s$ are broad and asymmetric in all samples, which indicate the existence of different oxygen groups. There are three main peaks in the spectra, which are related to C=O (531.6 eV), C=O aromatic or ZnO (530.7 eV), and C-O (533.0 eV) [42]. After comparing the Zn-MOF , **G1**, **G2**, **G3** and **G4** spectra in **Fig. 5e**, a slight increase of OC=O at 288.8 eV can be seen in samples **G1**, **G3** and **G4** because of Zn-MOF . $\text{N}1s$ spectra of the composites are shown in **Fig. S5b**. Samples of **G2 - G4** showed one broad asymmetrical peak, which suggested the presence of more than one type of nitrogen. Peaks appearing at 399.3 eV and 401.9 eV are related to the quinoid phenyl structure (NH-) and quaternary ammonium salt structure (C=N^+) coming from PANI component. **G2** also exhibited one peak at 397.5 eV, which is associated with pyridinic-N (C=N-) [43]. Thus, the XPS study reveals the formation of composite materials made of rGO, Zn-MOF , and PANI.

3.4. Cyclic voltammetry analysis

The electrochemical characteristics of the SC electrode are generally measured and determined using the cyclic voltammetry (CV) analysis to see if there is an improvement in the functionalities of samples. Usually, H₂SO₄ is used as an aqueous electrolyte in SC due to its high conductivity. It has been reported that carbon electrodes combined with PANI and GO have good electrochemical characteristics in the mentioned electrolyte [44–46]. In this study, CV analysis of the composite materials was investigated in 1 M H₂SO₄. The CV spectrum was measured at different scan rates from 5 to 100 mV/s in a fixed potential window of -0.2 to 0.8 V, as illustrated in **Fig. 6**.

From the CV spectra shown in **Fig. 6a**, the cathodic and anodic peaks can be seen to depict the redox process that occurred at all scan rates of **G1**. These curves reveal angular shapes at which the contribution of EDLC and the pseudocapacitance effect can be identified [8,47]. When adjusting scan rate to higher values, the oxidation peaks and anodic peaks are slightly shifted. This effect is caused by electric polarization, which can cause an irreversible reaction at very high sweep rates [48]. The CV curve of **G2** composite based on PANI and rGO shows two couple redox peaks indicating the presence of pseudocapacitive PANI [49].

The chemical representation of the different PANI structures respecting for the oxidation state is displayed in **Fig. S6a**. The appearance of redox peaks in **G2**, **G3**, and **G4** could be explained through the insertion and desertion of SO₄²⁻ ions (doping) in PANI according to equation (1):



where y is the doping degree, defined as the ratio between the number of charges in the polymer and the number of monomer units [50].

Additionally, PANI has a good conductivity property. It can be easily converted between various oxidation states like emeraldine, leucoemeraldine, and pernigraniline as shown in **Fig. S6**. As can be seen in **Fig. 6e**, the CV curves of **G2**, **G3**, and **G4** has two sets of discrete redox pairs of anodic and cathodic current peaks, which can show the particular activity in the acidic aqueous electrolyte. The first anodic peak in **Fig. 6e** occurring at the potential of 0.23 V of samples could be associated with doping of SO_4^{2-} anions. It can be related to the conversion of leucoemeraldine form of PANI to emeraldine salt (C1/A1). The next peak occurring at 0.52 V signifies the transition of emeraldine to fully oxidized pernigraniline state (C2/A2) (**Fig. S6b**) [51]. The C1 peaks of **G2** and **G3** are broader than that of **G4** possible due to the difference in the appearance of PANI (**Fig. 6e**). The aggregation of PANI(p) in **G2** may lead to low interaction with the SO_4^{2-} ions in the electrolyte during the redox reaction. As a consequence, the residual oxygenated groups of rGO could take place in the redox reaction. Meanwhile, as PANI was well dispersed in the structure of **G4**, it could support the reaction of C1/A1 [52].

3.5. Galvanostatic charge-discharge studies

The power density and specific capacitance of composite electrodes were investigated by chronopotentiometry technique. **Fig. 7** displays the Galvanostatic charge-discharge (GCD) curves of the composites in the aqueous electrolyte of 1 M H_2SO_4 (detailed values in **Table 2**). The measurements were carried out with varying current density ranges from 0.1 to 5 A/g and variable potential over time. The specific capacitance value was calculated as follows:

$$C_s = \frac{I \cdot \Delta t}{m \cdot \Delta V} \quad (2)$$

where I denotes the applied current (A), Δt is the time taken for the discharge, m is the mass of active electrode material, and ΔV is the discharge potential [29].

Fig. 7a and **b** exhibit the charge-discharge curves of **G1** and **G2**, respectively, tested in 1 M H₂SO₄ electrolyte at various current densities. It can be seen that the discharging process of **G2** required a longer time than **G1**. Accordingly, when PANI(p) is introduced to the composite using rGO, its presence causes a higher specific capacitance than a composite containing only Zn-MOF (**Fig. 7e**). The specific capacitance of **G2** at a current density of 0.1 A/g is 185.37 F/g, whereas, for **G1**, specific capacitance is 153.11 F/g. However, at the current densities of 0.2 A/g, both samples of **G1** and **G2** exhibit approximately the same specific capacitances, which are 132.83 F/g and 134.46 F/g, respectively. It can be seen that the capacitance of the electrodes made of **G2** decreases with an increasing scanning rate. At 5A/g, the capacitance of **G1** has a higher value of 91.9 F/g compared to 65.4 F/g of **G2**. Such a difference can be explained as follows. It is suggested that the porous structure of the materials is useful for ionic conductivity [53]. Since rGO, Zn-MOF, and PANI can provide electronic conductivity, the mass transport property of the electrode depends on the morphology of the materials and the nature of ions. Therefore, the capacitance of the electrode materials depends both on their structure and morphology. Notably, pores play a vital role in the ion transportation because the porous channels are able to overcome the limitations on the charged ion intercalation or adsorption [54].

When the sweep rates were increased during cycling, it caused a direct effect on the diffusion of electrolyte's ions into the matrix of the electrode. At higher rates, the ions could only reach the outer surface of the electrode materials. The material of **G2**, which contains aggregates of PANI(p) inside its structure, is characterized by the reduced size of pores and porous channels [55]. As a result, with an increase in the scanning rates, the electrolyte ions do not reach deep pores, which leads to a decrease in the pseudocapacitance of **G2**. The increase of the capacitance of **G3** (238.59 F/g) and **G4** (371.91 F/g) at 0.1 A/g scan rate is due to the good diffusion of Zn-MOF inside the

composites, where the porous crystallites contribute to the charging/discharging processes of electrodes. The combination of both Zn-MOF and PANI in the structures of **G3** and **G4** could allow the increase of ion transports, thus leading to higher capacitance at high scan rates compared to **G1** and **G2**. The large surface area of **G3** electrode may support the interaction between the electrolyte ions and material surface and let ions access the active regions. Nevertheless, the PANI thin layers in the **G4** composite could introduce better contact with electrolyte ions because of spreading out the charged structures, therefore facilitate conductivity during the scanning processes. Consequently, the capacitance of **G4** recorded at 5 A/g was measured to be 207.35 F/g compared to 130.15 F/g of **G3** at the same condition. The specific capacitance of this study and other supercapacitor electrodes based on different kinds of materials are compared and shown in **Table 3**. It can be noted that the composites made of rGO, Zn-MOF and PANI, showed a good specific capacitance at 0.1 A/g, especially for **G4**, when compared to the published results. Such a good electrochemical performance is mostly attributed to the contribution of PANI's pseudocapacitance and the combination of rGO and Zn-MOF.

3.6. Electrochemical impedance studies

Electrochemical impedance studies (EIS) were performed at an open circuit potential with an AC perturbation of 0.01 V in the frequency range from 0.01 Hz to 100 kHz to decipher the ion transport mechanism. **Fig. 8** shows the Nyquist plots and the equivalent circuit for the composites. The imaginary part Z'' is plotted against the real part Z' . The equivalent circuit consists of double-layer capacitance (C_{dl}), pseudocapacitance (C_p), equivalent resistance (R_s), charge transfer resistance (R_{ct}) and electron transfer resistance (R_{ect}). The shape of the curves demonstrates the pseudo-capacitive behavior of the electrode materials. The first distinct parts are semicircles in the

high-frequency region. The R_s of the electrolyte in contact with the current collector and electrode is represented at the beginning point of the semicircles [56,57]. The diameters of the semicircles represent the R_{ct} , which can signify the charge transfer rate at the electrode and electrolyte interface [58]. According to the Nyquist plot, R_{ct} of **G1**, **G2**, **G3** and **G4** were calculated to be 1.208 Ω , 0.986 Ω , 0.956 Ω , and 0.943 Ω , respectively. The low R_{ct} of **G3** and **G4** indicate the fast electron transport between the electrolyte and the samples, which could lead to higher capacitance retention [59]. The second part is shown as straight lines in the low-frequency region. This part is recognized as the Warburg impedance of diffusive resistance between the electrode material and electrolyte ions [59].

3.7. Electrochemical properties of symmetric supercapacitor

To discuss more the potential of the composites, the two-electrode supercapacitor cells based on **G1**, **G2**, **G3**, and **G4** were assembled in 1 M H₂SO₄ aqueous solution. The cells were characterized via CV, GCD and EIS. The CV curves of two-electrode of all cells measured at potential scan rates from 5 – 100 mV are display in **Fig.9** and **Fig. S7**. CV curves of **G1**, **G2**, and **G4** samples show slight curvature from the quasi rectangular shape. Those curves indicate the good capacitive behavior of the composites. Moreover, the **G3** CV curve shows the appearance of two redox peaks in the two electrode-system, which can be seen in the redox materials. As shown in **Fig. S7**, the increasing scan rate does not significantly affect the shape of CV curves. It indicates the good electron conductivity of the composites. By comparing the current response of the CV curves, **G4** exhibited the largest area following by **G3**, **G2**, and **G1**, respectively, thus indicating the higher specific capacitance of **G4**.

GCD curves of the composites characterized at different scan rates reveal the relative symmetrical and linear (**Fig. 9b**). The curves have exhibited the good electrochemical capacitive behavior of the cells. The specific capacitance of two-electrode SC value (C'_s) was calculated as follows:

$$C'_s = 2 \frac{I \cdot \Delta t}{m \cdot \Delta V} \quad (3)$$

The details of the specific capacitance of two-electrode SC cells are shown in **Fig. S8**, and **Table S1**. The results well agree with the curves of composites acquiring in three-electrode systems.

The EIS collected in the same frequency range of 0.01 Hz to 100 kHz at 0.01V for all devices was also carried out and shown in **Fig. 9d**. Compared to the results displayed in EIS study of three-electrode system, the Nyquist plots of two-electrode cells exhibit a similar straight line in the low-frequency region. The R_{ct} of **G4** still has the smallest value indicating the device's better capacitance behavior [59].

3.8. Cyclic stability

Fig. 10 shows the four samples' cycling stability performances at the current density of 1 A/g for 5000 cycles in a two-electrode symmetrical SC. Compared to the other samples, **G2** appears to have lower charge-discharge stability; its specific capacitance decreases gradually with time. After 5000 charge/discharge cycles, its capacitance retention was measured at 77.18%. The low electron transport expressed via the higher R_{ct} in EIS study can explain the poor cycle stability. Furthermore, in the doping/dedoping process, the volumetric performance of PANI was significantly changed, leading to mechanical degradation, which could involve the stability of the composite [17]. Higher R_{ct} of **G1** compared to **G2** may lead to lower capacitance retention after the period. However, the firmed crystalline structure of Zn-MOF has not been affected during the

testing times, which could explain why the capacitance retention of **G1** was 79.53% after a long period. In case of the composites containing both such as **G3** and **G4**, the capacitance retentions were higher than the others at 82% and 81.1 %, respectively. This rise can be explained by the stability and the solidity of the whole structure when combining three constituents. The PANI morphologies caused the different interaction among each component in **G3** and **G4**. The Zn-MOF reinforced the steadiness of material frameworks and compensated for the less mechanical stability of the thin-layer PANI affected by the charge/discharge process. It explains the reason why the specific capacitance of **G4** was good in but its retention decreased gradually according to times. In contrast, the **G3** work dropped quickly after 200 cycles and then gained the stable level after 800 cycles. The **G3** composited of granule PANI, Zn-MOF powder and rGO aerogel may have better pathway for electrolyte ions to contact the surface of materials and thus need the initial stability.

4. Conclusion

Instead of using single materials, the combination of rGO with conducting PANI and Zn-MOF used in our research has offered a good performance beyond the limitations of individual components. Therefore, composite materials based on rGO, PANI, and Zn-MOF have been fabricated via different methods related to the polymerization processes. The rGO component provides porous conductive support with the π -conjugated system spreading out the carbon backbones combined with the crystalline structure of Zn-MOF for the composites. The addition of PANI into the composite facilitates charge transfer between electrolyte and electrodes, which results in the specific capacity increment of ca 372 F/g at a current density of 0.1 A/g. The improved performance can be attributed to the enhanced electronic conductivity, higher

pseudocapacitance behavior, and porous morphology of the created structures, which can provide efficient ions transfer. The results reveal that the composites containing Zn-MOF appear to have better stability due to its crystalline structure, which can be maintained during a long time of the charge/discharge process. As a consequence of higher specific capacity and better cycle stability, the composites based on rGO, PANI, and Zn-MOF developed in our study appear to be suitable potential electrode materials for SC applications.

Acknowledgments

This work was supported by the Ministry of Education, Youth and Sports of the Czech Republic – DKRVO (RP/CPS/2020/005)

References

- [1] C. Xu, B. Xu, Y. Gu, Z. Xiong, J. Sun, X.S. Zhao, Graphene-based electrodes for electrochemical energy storage, *Energy Environ. Sci.* 6 (2013) 1388. doi:10.1039/c3ee23870a.
- [2] C. Zhao, W. Zheng, A Review for Aqueous Electrochemical Supercapacitors, *Front. Energy Res.* 3 (2015) 1–11. doi:10.3389/fenrg.2015.00023.
- [3] K. Ma, X. Liu, Q. Cheng, P. Saha, H. Jiang, C. Li, Flexible textile electrode with high areal capacity from hierarchical V₂O₅ nanosheet arrays, *J. Power Sources.* 357 (2017) 71–76. doi:10.1016/j.jpowsour.2017.04.105.
- [4] Y. Gao, Graphene and Polymer Composites for Supercapacitor Applications: a Review, *Nanoscale Res. Lett.* 12 (2017) 387. doi:10.1186/s11671-017-2150-5.
- [5] W. Wei, X. Cui, W. Chen, D.G. Ivey, Manganese oxide-based materials as electrochemical supercapacitor electrodes, *Chem. Soc. Rev.* 40 (2011) 1697–1721.

- doi:10.1039/C0CS00127A.
- [6] A. González, E. Goikolea, J.A. Barrena, R. Mysyk, Review on supercapacitors: Technologies and materials, *Renew. Sustain. Energy Rev.* 58 (2016) 1189–1206. doi:10.1016/j.rser.2015.12.249.
- [7] Patrice Simon, Yury Gogotsi, Materials for electrochemical capacitors, *Nat. Mater.* 7 (2008) 845–854. doi:10.1038/nmat2297.
- [8] Q. Cheng, J. Tang, J. Ma, H. Zhang, N. Shinya, L.C. Qin, Polyaniline-coated electro-etched carbon fiber cloth electrodes for supercapacitors, *J. Phys. Chem. C.* 115 (2011) 23584–23590. doi:10.1021/jp203852p.
- [9] Y. Wang, J. Guo, T. Wang, J. Shao, D. Wang, Y.W. Yang, Mesoporous transition metal oxides for supercapacitors, *Nanomaterials.* 5 (2015) 1667–1689. doi:10.3390/nano5041667.
- [10] V.C. Tran, S. Sahoo, J. Hwang, V.Q. Nguyen, J.-J. Shim, Poly(aniline-co-pyrrole)-spaced graphene aerogel for advanced supercapacitor electrodes, *J. Electroanal. Chem.* 810 (2018) 154–160. doi:10.1016/j.jelechem.2018.01.011.
- [11] X. Li, L. Zhi, Graphene hybridization for energy storage applications, *Chem. Soc. Rev.* 47 (2018) 3189–3216. doi:10.1039/c7cs00871f.
- [12] N. Kumar, P.K. Sahoo, H.S. Panda, Enriched Doping Level and Tuned Fiber Fractal Dimensions in Nonwoven Carbon-Doped Polyaniline for Efficient Solid-State Supercapacitors, *Energy Technol.* 5 (2017) 253–266. doi:10.1002/ente.201600239.
- [13] A. Borenstein, O. Hanna, R. Attias, S. Luski, T. Brousse, D. Aurbach, Carbon-based composite materials for supercapacitor electrodes: A review, *J. Mater. Chem. A.* 5 (2017) 12653–12672. doi:10.1039/c7ta00863e.

- [14] C. Su, G. Wang, F. Huang, Y. Sun, Effect of carbon black modified with polyaniline on resistivity behavior of polyethylene/carbon black composites, *J. Macromol. Sci. Part B Phys.* 47 (2008) 65–75. doi:10.1080/15568310701744158.
- [15] P. Lv, X. Tang, R. Zheng, X. Ma, K. Yu, W. Wei, Graphene/Polyaniline Aerogel with Superelasticity and High Capacitance as Highly Compression-Tolerant Supercapacitor Electrode, *Nanoscale Res. Lett.* 12 (2017). doi:10.1186/s11671-017-2395-z.
- [16] H.P. Cong, X.C. Ren, P. Wang, S.H. Yu, Flexible graphene-polyaniline composite paper for high-performance supercapacitor, *Energy Environ. Sci.* 6 (2013) 1185–1191. doi:10.1039/c2ee24203f.
- [17] L. Li, A.R.O. Raji, H. Fei, Y. Yang, E.L.G. Samuel, J.M. Tour, Nanocomposite of polyaniline nanorods grown on graphene nanoribbons for highly capacitive pseudocapacitors, *ACS Appl. Mater. Interfaces.* 5 (2013) 6622–6627. doi:10.1021/am4013165.
- [18] Z. Wang, J. Huang, Z. Guo, X. Dong, Y. Liu, Y. Wang, Y. Xia, A Metal-Organic Framework Host for Highly Reversible Dendrite-free Zinc Metal Anodes, *Joule.* 3 (2019) 1289–1300. doi:10.1016/j.joule.2019.02.012.
- [19] L. Ma, C. Abney, W. Lin, Enantioselective catalysis with homochiral metal-organic frameworks, *Chem. Soc. Rev.* 38 (2009) 1248–1256. doi:10.1039/b807083k.
- [20] Y. Gong, J. Li, P.G. Jiang, Q.F. Li, J.H. Lin, Novel metal(ii) coordination polymers based on N,N'-bis-(4-pyridyl) phthalamide as supercapacitor electrode materials in an aqueous electrolyte, *Dalt. Trans.* 42 (2013) 1603–1611. doi:10.1039/c2dt31965a.
- [21] K.M. Choi, H.M. Jeong, J.H. Park, Y.B. Zhang, J.K. Kang, O.M. Yaghi, Supercapacitors of nanocrystalline metal-organic frameworks, *ACS Nano.* 8 (2014) 7451–7457.

doi:10.1021/nm5027092.

- [22] N. Campagnol, R. Romero-Vara, W. Deleu, L. Stappers, K. Binnemans, D.E. De Vos, J. Fransaer, A Hybrid Supercapacitor based on Porous Carbon and the Metal-Organic Framework MIL-100(Fe), *ChemElectroChem*. 1 (2014) 1182–1188.
doi:10.1002/celec.201402022.
- [23] D.Y. Lee, S.J. Yoon, N.K. Shrestha, S.H. Lee, H. Ahn, S.H. Han, Unusual energy storage and charge retention in Co-based metal-organic-frameworks, *Microporous Mesoporous Mater.* 153 (2012) 163–165. doi:10.1016/j.micromeso.2011.12.040.
- [24] M. Du, M. Chen, X.G. Yang, J. Wen, X. Wang, S.M. Fang, C. Sen Liu, A channel-type mesoporous In(iii)-carboxylate coordination framework with high physicochemical stability for use as an electrode material in supercapacitors, *J. Mater. Chem. A*. 2 (2014) 9828–9834. doi:10.1039/c4ta00963k.
- [25] S. Sundriyal, S. Mishra, A. Deep, Study of manganese-1,4-benzenedicarboxylate metal organic framework electrodes based solid state symmetrical supercapacitor, *Energy Procedia*. 158 (2019) 5817–5824. doi:10.1016/j.egypro.2019.01.546.
- [26] N.A. Jalil, M.A.A. Mohd Abdah, N.H.N. Azman, Y. Sulaiman, Polyaniline and manganese oxide decorated on carbon nanofibers as a superior electrode material for supercapacitor, *J. Electroanal. Chem.* 867 (2020) 114188.
doi:10.1016/j.jelechem.2020.114188.
- [27] P. Yang, X. Xiao, Y. Li, Y. Ding, P. Qiang, X. Tan, W. Mai, Z. Lin, W. Wu, T. Li, H. Jin, P. Liu, J. Zhou, C.P. Wong, Z.L. Wang, Hydrogenated ZnO core-shell nanocables for flexible supercapacitors and self-powered systems, *ACS Nano*. 7 (2013) 2617–2626.
doi:10.1021/nm306044d.

- [28] Y. Jiao, J. Pei, D. Chen, C. Yan, Y. Hu, Q. Zhang, G. Chen, Mixed-metallic MOF based electrode materials for high performance hybrid supercapacitors, *J. Mater. Chem. A* 5 (2017) 1094–1102. doi:10.1039/C6TA09805C.
- [29] Q.B. Le, E. Vargun, H. Fei, Q. Cheng, C. Bubulinca, R. Moučka, I. Sapurina, T.D. Tran, N.E. Kazantseva, P. Saha, Effect of PANI and PPy on Electrochemical Performance of rGO/ZnMn₂O₄ Aerogels as Electrodes for Supercapacitors, *J. Electron. Mater.* 49 (2020) 4697–4706. doi:10.1007/s11664-020-08198-4.
- [30] G. Wang, L. Jin, J. Ye, X. Li, Electrical and electrochemical properties of poly(2,5-dimercapto-1,3,4-thiadiazole)-polyaniline adduct intercalated graphite oxide composites, *Mater. Chem. Phys.* 122 (2010) 224–229. doi:10.1016/j.matchemphys.2010.02.038.
- [31] H.M. Yang, X.L. Song, T.L. Yang, Z.H. Liang, C.M. Fan, X.G. Hao, Electrochemical synthesis of flower shaped morphology MOFs in an ionic liquid system and their electrocatalytic application to the hydrogen evolution reaction, *RSC Adv.* 4 (2014) 15720–15726. doi:10.1039/c3ra47744d.
- [32] A.K. Chaudhari, B.E. Souza, J.C. Tan, Electrochromic thin films of Zn-based MOF-74 nanocrystals facilely grown on flexible conducting substrates at room temperature, *APL Mater.* 7 (2019). doi:10.1063/1.5108948.
- [33] B. Manna, S. Sharma, S.K. Ghosh, Synthesis and crystal structure of a Zn(II)-based MOF bearing neutral N-donor linker and SiF₆²⁻ anion, *Crystals* 8 (2018). doi:10.3390/cryst8010037.
- [34] L.N. Zhu, L.Z. Zhang, W.Z. Wang, D.Z. Liao, P. Cheng, Z.H. Jiang, S.P. Yan, [Zn(BDC)(H₂O)₂]_n: A novel blue luminescent coordination polymer constructed from BDC-bridged 1-D chains via interchain hydrogen bonds (BDC = 1,4-

- benzenedicarboxylate), *Inorg. Chem. Commun.* 5 (2002) 1017–1021. doi:10.1016/S1387-7003(02)00634-2.
- [35] Q. Shao, J. Tang, Y. Lin, J. Li, F. Qin, J. Yuan, L.C. Qin, Carbon nanotube spaced graphene aerogels with enhanced capacitance in aqueous and ionic liquid electrolytes, *J. Power Sources.* 278 (2015) 751–759. doi:10.1016/j.jpowsour.2014.12.052.
- [36] A. Alazmi, O. El Tall, S. Rasul, M.N. Hedhili, S.P. Patole, P.M.F.J. Costa, A process to enhance the specific surface area and capacitance of hydrothermally reduced graphene oxide, *Nanoscale.* 8 (2016) 17782–17787. doi:10.1039/c6nr04426c.
- [37] N. Arjun, K. Uma, G.T. Pan, T.C.K. Yang, G. Sharmila, One-pot synthesis of covalently functionalized reduced graphene oxide–polyaniline nanocomposite for supercapacitor applications, *Clean Technol. Environ. Policy.* 20 (2018) 2025–2035. doi:10.1007/s10098-018-1573-8.
- [38] F.P. Du, N.N. Cao, Y.F. Zhang, P. Fu, Y.G. Wu, Z.D. Lin, R. Shi, A. Amini, C. Cheng, PEDOT:PSS/graphene quantum dots films with enhanced thermoelectric properties via strong interfacial interaction and phase separation, *Sci. Rep.* 8 (2018) 1–12. doi:10.1038/s41598-018-24632-4.
- [39] M. Li, X. Huang, C. Wu, H. Xu, P. Jiang, T. Tanaka, Fabrication of two-dimensional hybrid sheets by decorating insulating PANI on reduced graphene oxide for polymer nanocomposites with low dielectric loss and high dielectric constant, *J. Mater. Chem.* 22 (2012) 23477–23484. doi:10.1039/c2jm34683d.
- [40] Y. Wu, X. Song, J. Zhang, S. Xu, N. Xu, H. Yang, Y. Miao, L. Gao, J. Zhang, G. Xiao, Zn₂(C₉H₃O₆)(C₄H₅N₂)(C₄H₆N₂)₃ MOF as a highly efficient catalyst for chemical fixation of CO₂ into cyclic carbonates and kinetic studies, *Chem. Eng. Res. Des.* 140

- (2018) 273–282. doi:10.1016/j.cherd.2018.10.034.
- [41] S.H. Patil, A.P. Gaikwad, S.D. Sathaye, K.R. Patil, To form layer by layer composite film in view of its application as supercapacitor electrode by exploiting the techniques of thin films formation just around the corner, *Electrochim. Acta.* 265 (2018) 556–568. doi:10.1016/j.electacta.2018.01.165.
- [42] H. Hantsche, High resolution XPS of organic polymers, the scienta ESCA300 database. By G. Beamson and D. Briggs, Wiley, Chichester 1992, 295 pp., hardcover, £ 65.00, ISBN 0-471-93592-1, 1993. doi:10.1002/adma.19930051035.
- [43] P. Xiong, Q. Chen, M. He, X. Sun, X. Wang, Cobalt ferrite-polyaniline heteroarchitecture: A magnetically recyclable photocatalyst with highly enhanced performances, *J. Mater. Chem.* 22 (2012) 17485–17493. doi:10.1039/c2jm31522j.
- [44] P. Sekar, B. Anothumakkool, S. Kurungot, 3D Polyaniline Porous Layer Anchored Pillared Graphene Sheets: Enhanced Interface Joined with High Conductivity for Better Charge Storage Applications, *ACS Appl. Mater. Interfaces.* 7 (2015) 7661–7669. doi:10.1021/acsami.5b00504.
- [45] H. Xu, H. Jiang, X. Li, G. Wang, Synthesis and electrochemical capacitance performance of polyaniline doped with lignosulfonate, *RSC Adv.* 5 (2015) 76116–76121. doi:10.1039/c5ra12292a.
- [46] H. Fei, N. Saha, N. Kazantseva, T. Babkova, M. Machovsky, G. Wang, H. Bao, P. Saha, Polyaniline/reduced graphene oxide hydrogel film with attached graphite current collector for flexible supercapacitors, *J. Mater. Sci. Mater. Electron.* 29 (2018) 3025–3034. doi:10.1007/s10854-017-8233-3.
- [47] X. Li, H. Song, Y. Zhang, H. Wang, K. Du, H. Li, Y. Yuan, J. Huang, Enhanced

- electrochemical capacitance of graphene nanosheets coating with polyaniline for supercapacitors, *Int. J. Electrochem. Sci.* 7 (2012) 5163–5171.
- [48] P.E. Saranya, S. Selladurai, Efficient electrochemical performance of ZnMn₂O₄ nanoparticles with rGO nanosheets for electrodes in supercapacitor applications, *J. Mater. Sci. Mater. Electron.* 29 (2018) 3326–3339. doi:10.1007/s10854-017-8268-5.
- [49] D. Wang, F. Li, J. Zhao, W. Ren, Z. Chen, J. Tan, Z. Wu, I. Gentle, G.Q. Lu, H. Cheng, Fabrication of Graphene/Polyaniline Composite Paper via In Situ Anodic Electropolymerization for High-Performance Flexible Electrode, *ACS Nano.* 3 (2009) 1745–1752. doi:10.1021/nn900297m.
- [50] B. Jugović, M. Gvozdrenović, J. Stevanović, T. Trišović, B. Grgur, Characterization of electrochemically synthesized PANI on graphite electrode for potential use in electrochemical power sources, *Mater. Chem. Phys.* 114 (2009) 939–942. doi:10.1016/j.matchemphys.2008.10.069.
- [51] N. Gospodinova, L. Terlemezyan, Conducting polymers prepared by oxidative polymerization: Polyaniline, *Prog. Polym. Sci.* 23 (1998) 1443–1484. doi:10.1016/S0079-6700(98)00008-2.
- [52] Q. Zhou, Y. Li, L. Huang, C. Li, G. Shi, Three-dimensional porous graphene/polyaniline composites for high-rate electrochemical capacitors, *J. Mater. Chem. A.* 2 (2014) 17489–17494. doi:10.1039/c4ta03639e.
- [53] J. Shabani Shayeh, P. Norouzi, M.R. Ganjali, Studying the supercapacitive behavior of a polyaniline/nano-structural manganese dioxide composite using fast Fourier transform continuous cyclic voltammetry, *RSC Adv.* 5 (2015) 20446–20452. doi:10.1039/c4ra16801a.

- [54] T. Brousse, M. Toupin, R. Dugas, L. Athouël, O. Crosnier, D. Bélanger, Crystalline MnO₂ as Possible Alternatives to Amorphous Compounds in Electrochemical Supercapacitors, *J. Electrochem. Soc.* 153 (2006) A2171. doi:10.1149/1.2352197.
- [55] L. Vast, L. Carpentier, F. Lallemand, J.F. Colomer, G. Van Tendeloo, A. Fonseca, J.B. Nagy, Z. Mekhalif, J. Delhalle, Multiwalled carbon nanotubes functionalized with 7-octenyltrichlorosilane and n-octyltrichlorosilane: Dispersion in Sylgard®184 silicone and Young's modulus, *J. Mater. Sci.* 44 (2009) 3476–3482. doi:10.1007/s10853-009-3464-1.
- [56] M.D. Stoller, R.S. Ruoff, Best practice methods for determining an electrode material's performance for ultracapacitors, *Energy Environ. Sci.* 3 (2010) 1294–1301. doi:10.1039/c0ee00074d.
- [57] Y.S. Lim, Y.P. Tan, H.N. Lim, N.M. Huang, W.T. Tan, Preparation and characterization of polypyrrole/graphene nanocomposite films and their electrochemical performance, *J. Polym. Res.* 20 (2013) 156. doi:10.1007/s10965-013-0156-y.
- [58] H. Du, Y. Xie, C. Xia, W. Wang, F. Tian, Electrochemical capacitance of polypyrrole-titanium nitride and polypyrrole-titania nanotube hybrids, *New J. Chem.* 38 (2014) 1284–1293. doi:10.1039/c3nj01286g.
- [59] M. Li, J.P. Cheng, J. Wang, F. Liu, X.B. Zhang, The growth of nickel-manganese and cobalt-manganese layered double hydroxides on reduced graphene oxide for supercapacitor, *Electrochim. Acta.* 206 (2016) 108–115. doi:10.1016/j.electacta.2016.04.084.
- [60] D.Y. Lee, D. V. Shinde, E.K. Kim, W. Lee, I.W. Oh, N.K. Shrestha, J.K. Lee, S.H. Han, Supercapacitive property of metal-organic-frameworks with different pore dimensions and morphology, *Microporous Mesoporous Mater.* 171 (2013) 53–57.

doi:10.1016/j.micromeso.2012.12.039.

- [61] G. Zhu, H. Wen, M. Ma, W. Wang, L. Yang, L. Wang, X. Shi, X. Cheng, X. Sun, Y. Yao, A self-supported hierarchical Co-MOF as a supercapacitor electrode with ultrahigh areal capacitance and excellent rate performance, *Chem. Commun.* 54 (2018) 10499–10502.

doi:10.1039/c8cc03669a.

Table Captions

Table 1: The elemental composition of prepared hybrids as determined by EDX-XRF method.

Table 2: The specific capacitance of the electrodes made of composites at different rates.

Table 3: Comparison of the specific capacitance of composites obtained in this study with reported literature.

Figure Captions

Figure 1. SEM images of (a) G1; (b) G2; (c) G3 and (d) G4; TEM images of (e), (f) G1; (g), (h) G2; (i), (j) G3 and (k), (l) G4.

Figure 2. BET data of composite materials G1, G2, G3 and G4.

Figure 3. FTIR spectra of (a) Zn-MOF and PANI(p), and (b) G1, G2, G3 and G4.

Figure 4. TGA spectra G1, G2, G3 and G4.

Figure 5. XPS spectra of (a) survey spectrum (b) C1s, and (c) O1s of G1, G2, G3 and G4.

Figure 6. Cyclic voltammetry of (a) G1, (b) G2, (c) G3, (d) G4, and (e) all samples at 5 mV/s.

Figure 7. Charge-discharge plots of (a) G1, (b) G2, (c) G3, (d) G4, (e) all samples at 0.1 A/g and (f) their specific capacitance calculated from galvanostatic curves

Figure 8. Electrical impedance spectra in 1 M H₂SO₄ of G1, G2, G3 and G4.

Figure 9. Two-electrode supercapacitor performance of (a) cyclic voltammetry at 5 mV/s, (b) charge-discharge plots at 0.1 A/g, (c) specific capacitance calculated from galvanostatic curves, and (d) electrical impedance.

Figure 10. The cyclic capacity retention during 5000 cycles at 1 A/g.

Table caption of Supplementary.

Table S1: The specific capacitance at different scan rates of 2-electrode supercapacitor cells.

Figure Captions of Supplementary

Figure S1. SEM images of (a) PANI(p) and (b) Zn-MOF.

Figure S2. (a) XRD spectra of Zn-MOF and (b) The molecular structure and atom-labeling scheme of Zn-MOF.

Figure S3. Elemental analysis spectrum of rGO/Zn-MOF (**G1**), rGO/PANI(p) (**G2**), rGO/PANI(p)/Zn-MOF (**G3**) and rGO/Zn-MOF@PANI (**G4**).

Figure S4. XPS spectra of (a) survey spectrum (b) Zn 2p, (c) C 1s and (d) O1s of Zn-MOF and (e) ZnO Auger peak.

Figure S5. XPS spectra of (a) Zn 2p of **G1**, **G3**, and **G4** and (b) N 1s of **G2**, **G3**, and **G4**.

Figure S6. (a) CV curve of **G4** at 5 mV/s scan rate and (b) schematic chemical representation of oxidation states of PANI.

Figure S7. Cyclic voltammetry from 5 – 100 mV/s of two-electrode supercapacitor cells made of **G1**, **G2**, **G3**, and **G4**.

Figure S8. Charge-discharge plots of two-electrode supercapacitor cells made of **G1**, **G2**, **G3**, and **G4**.

Table 1

The elemental composition of prepared hybrids as determined by EDX-XRF method.

Samples	C(%)	H(%)	N(%)
G1	75.06 ± 4.06	0.81 ± 0.04	0
G2	86.83 ± 3.44	0.74 ± 0.03	1.63 ± 0.06
G3	75.95 ± 0.42	1.24 ± 0.14	1.80 ± 0.53
G4	76.69 ± 0.17	0.87 ± 0.02	0.50 ± 0.05

Table 2

The specific capacitance of the electrodes made of composites at different rates

Scan rate (A/g)	Specific capacitance (F/g)			
	G1	G2	G3	G4
0.1	153.11	185.37	238.59	371.91
0.2	132.83	134.46	223.75	291.87
0.5	119.94	110.63	185.67	253.35
1	111.18	96.91	168.1	237.7
1.5	107.36	88.25	158.88	229.26
2	103.7	82.52	151.46	223.48
2.5	100.78	78.15	146.58	216.36
3	98.58	74.97	142.47	212.4
4	94.92	69.44	136.09	211.36
5	91.9	65.4	130.15	207.35

Table 3

Comparison of the specific capacitance of composites obtained in this study with reported literature.

No.	Compound	Specific capacitance	Scan rate	Reference No.
1	Mn-MOF/CB	177.90 F/g	0.5 A/g	[25]
2	Co-MOF film	206.76 F/g	0.6 A/g	[23]
3	Co-BPDC	179.20 F/g	10 mV/s	[60]
4	rGO/ZnMn ₂ O ₄ @PANI	297.80 F/g	0.2 A/g	[29]
5	Zn/Ni-MOF	161.50 F/g	1 A/g	[28]
6	Co-MOF/NF	13.6 F/cm ²	2 mA/cm ²	[61]
7	rGO/Zn-MOF@PANI	371.91 F/g	0.1 A/g	This study

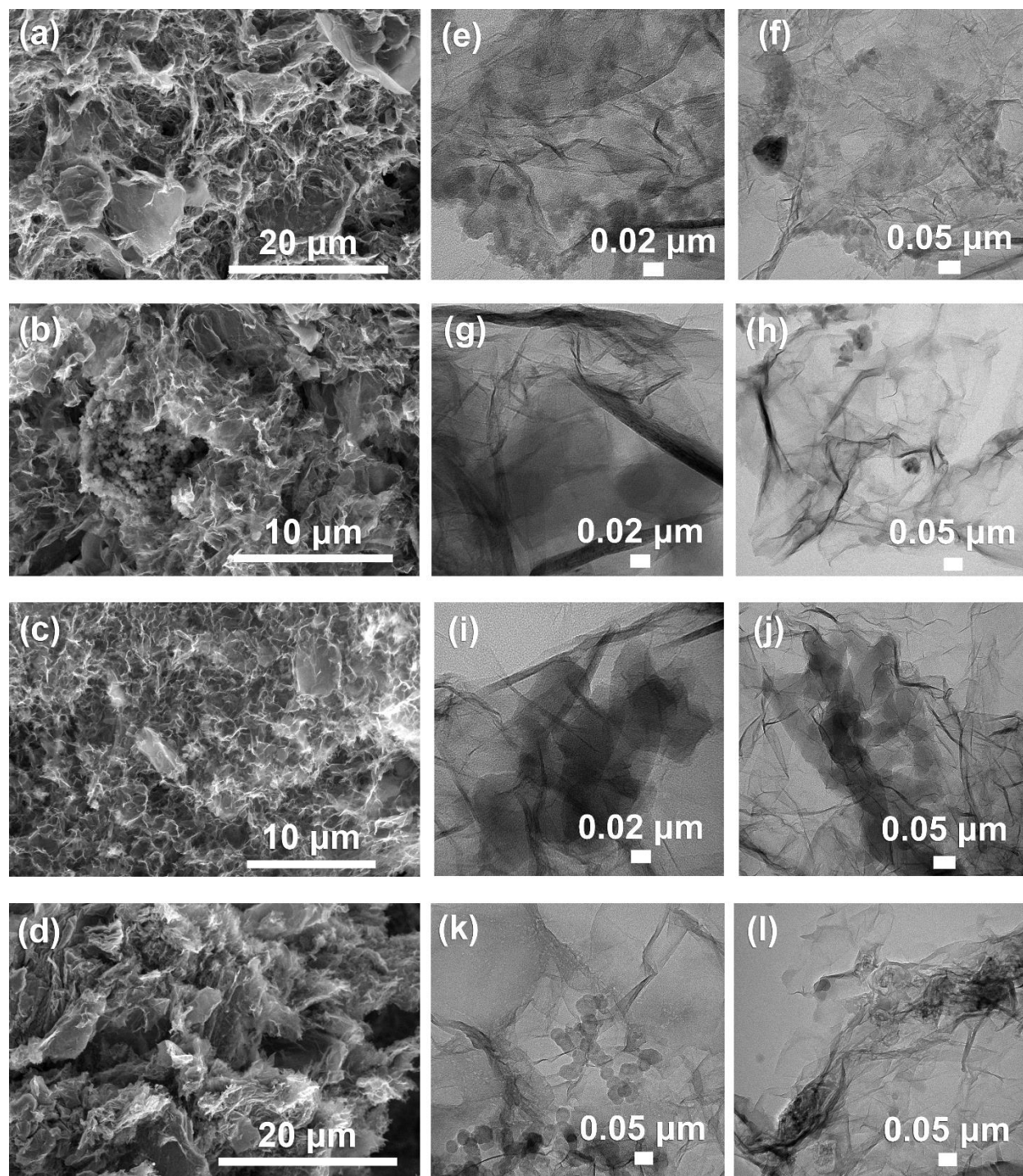


Figure 1. SEM images of (a) G1; (b) G2; (c) G3 and (d) G4; TEM images of (e), (f) G1; (g), (h) G2; (i), (j) G3 and (k), (l) G4.

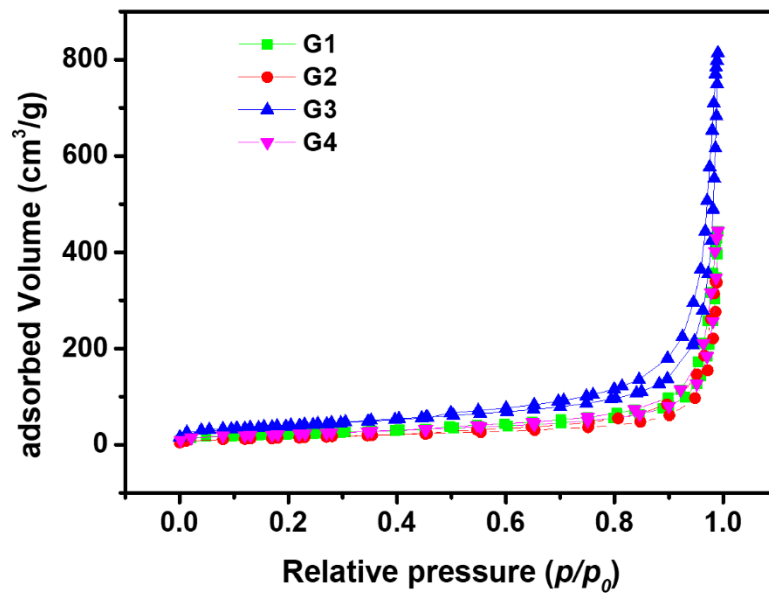


Figure 2. BET data of composite materials G1, G2, G3 and G4.

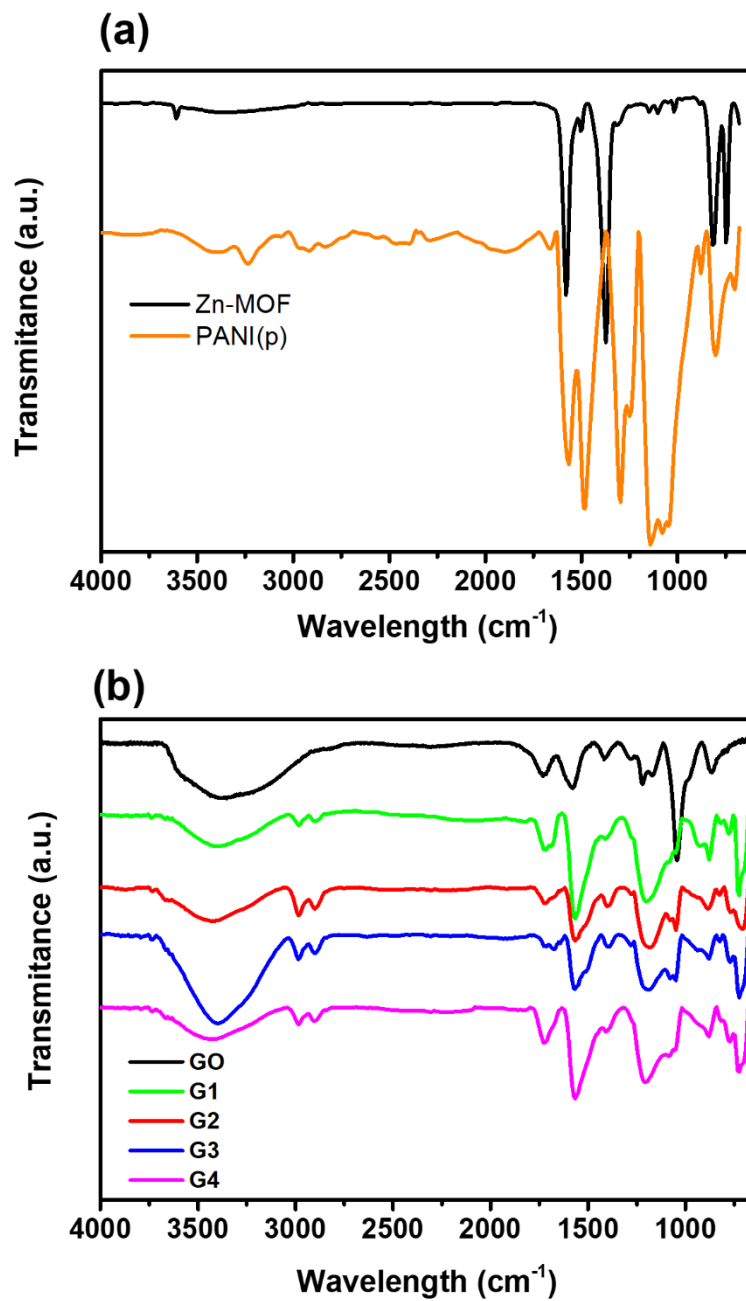


Figure 3. FTIR spectra of (a) Zn-MOF and PANI(p) and (b) G1, G2, G3 and G4.

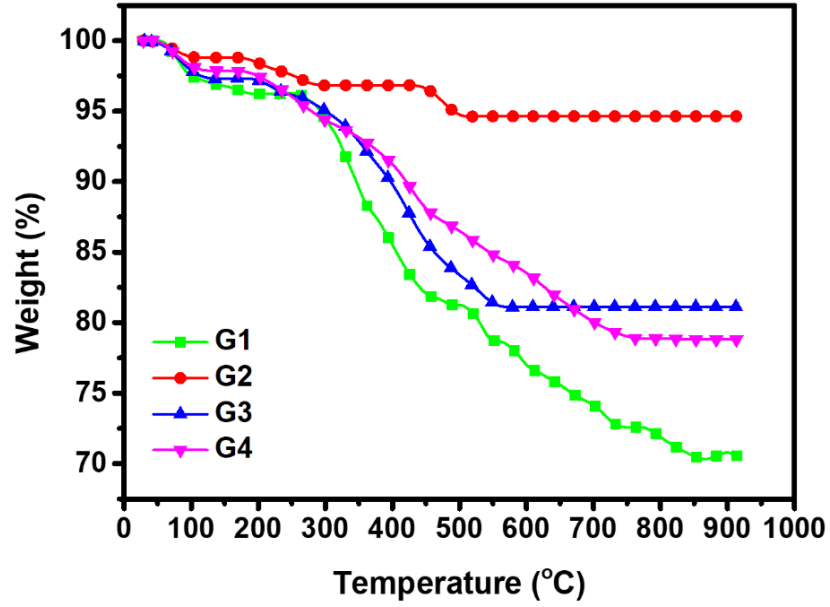


Figure 4. TGA spectra G1, G2, G3 and G4.

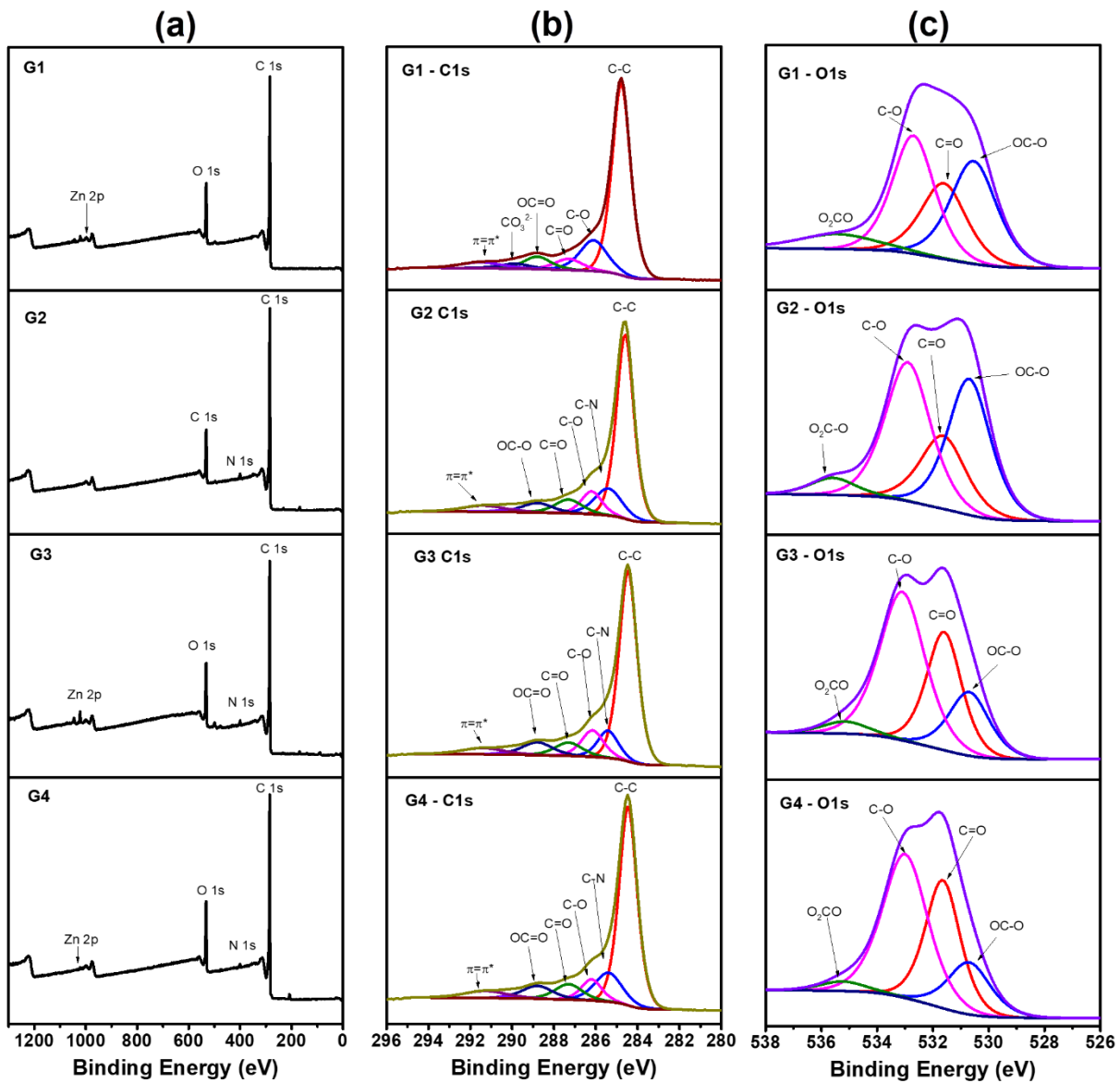


Figure 5. XPS spectra of (a) survey spectrum (b) C1s and (c) O1s of G1, G2, G3 and G4

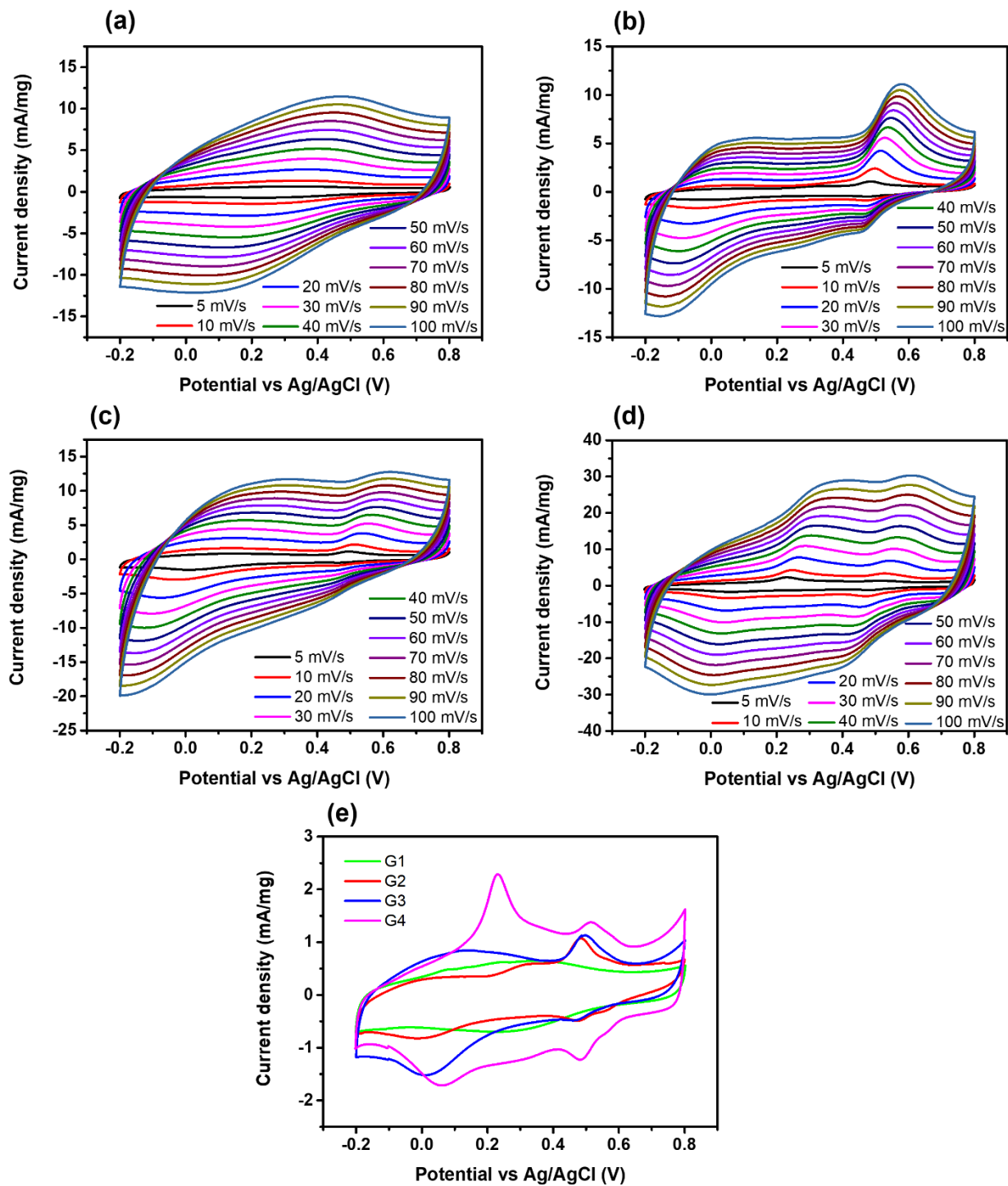


Figure 6. Cyclic voltammetry of (a) G1, (b) G2, (c) G3, (d) G4 and (e) all samples at 5 mV/s.

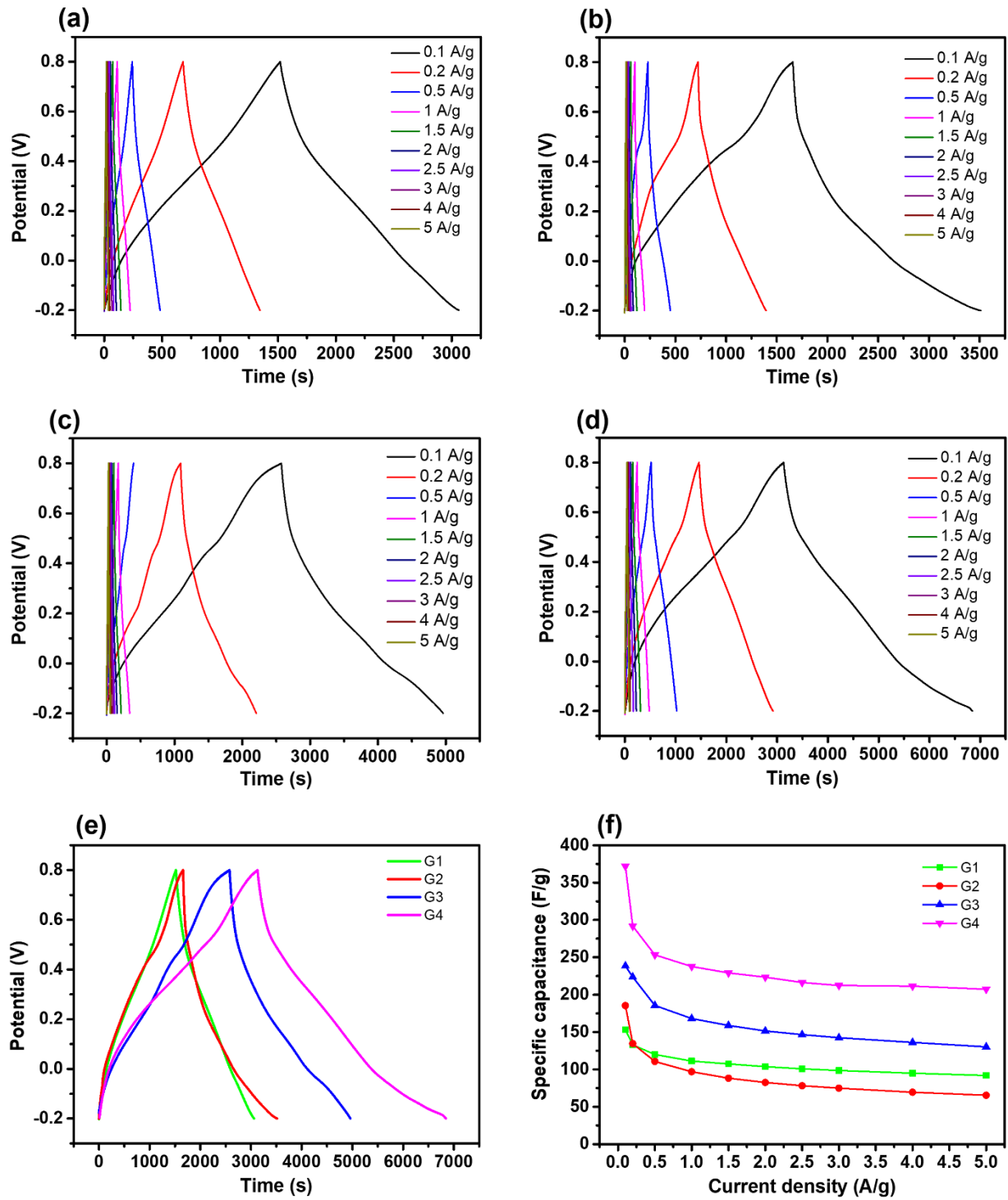


Figure 7. Charge-discharge plots of (a) G1, (b) G2, (c) G3, (d) G4, (e) all samples at 0.1 A/g and (f) their specific capacitance calculated from galvanostatic curves.

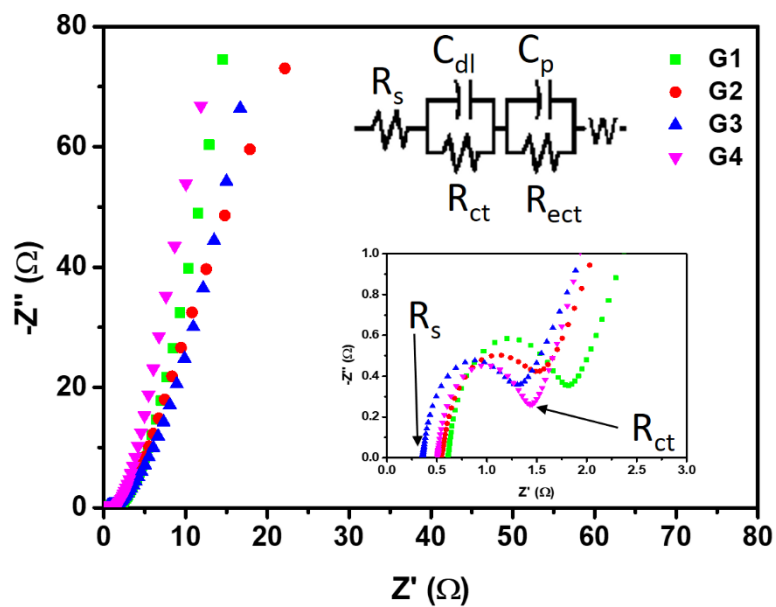


Figure 8. Electrical impedance spectra in 1 M H₂SO₄ of **G1**, **G2**, **G3** and **G4**.

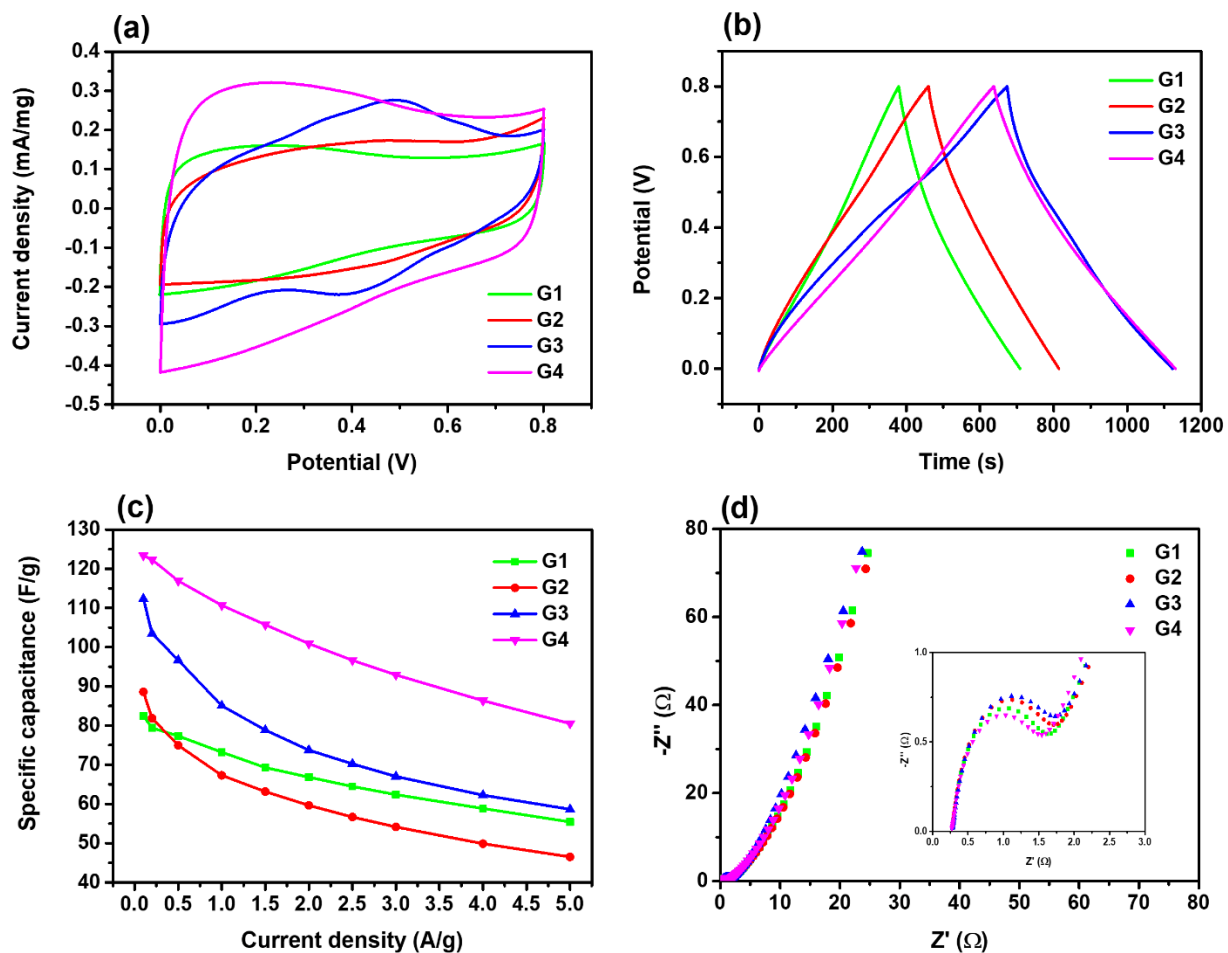


Figure 9. Two-electrode supercapacitor performance of (a) cyclic voltammety at 5 mV/s, (b) charge-discharge plots at 0.1 A/g, (c) specific capacitance calculated from galvanostatic curves, and (d) electrical impedance.

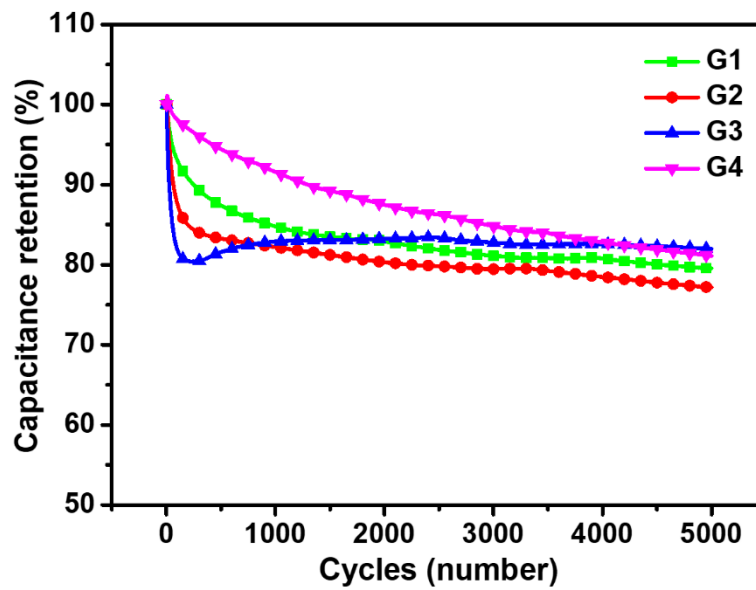


Figure 10. The cyclic capacity retention during 5000 cycles at 1 A/g.